J Mater Sci: Mater Electron (2020) 31:17491–17501

Effect of $BiAlO_3$ doping on dielectric and ferroelectric properties of $(Bi_{0.5}Na_{0.42}K_{0.08})_{0.96}Sr_{0.04}Ti_{0.975}Nb_{0.025}O_3$ lead-free ceramics

Xin Liu[1], Xiao-ming Chen[1,*], Li-na Liu[1], and Guang-bin Zhang[1,*]

[1] *Shaanxi Key Laboratory of Ultrasonics, School of Physics and Information Technology, Shaanxi Normal University, 710119 Xi'an, People's Republic of China*

Received: 25 April 2020
Accepted: 21 August 2020
Published online: 2 September 2020

ABSTRACT

The $(1-x)(Bi_{0.5}Na_{0.42}K_{0.08})_{0.96}Sr_{0.04}Ti_{0.975}Nb_{0.025}O_3$–$xBiAlO_3$ (x = 0, 0.01, 0.02, 0.03, 0.05) lead-free ceramics were synthesized by means of the traditional solid-state reaction method. Influences of the $BiAlO_3$ doping on structure, dielectric, and ferroelectric properties of the ceramics were systematically investigated. The X-ray diffraction (XRD) measurement was used to detect phase structure. The samples exhibit pseudocubic symmetry and dense microstructures. All of the ceramics, whether they were poled or unpoled, exhibit two dielectric anomalies on the dielectric spectra between room temperature and 350 °C, and no dielectric anomaly related to depolarization behavior was observed. The polarization loops and strain curves exhibit pinching-type shape and sprout shape, respectively. The corresponding mechanism was also discussed.

1 Introduction

Piezoelectric materials are important for the application of transducers. As traditional transducer materials, Pb(Zr,Ti)$O_3$and $PbMg_{1/3}Nb_{2/3}O_3$-$PbTiO_3$-based ceramics have been widely investigated in the field of various electromechanical applications [1–3]. However, taking into account irreversible ecological and health issues caused by lead-based components, lead-free materials with alternative properties have been widely studied. Excellent electrical properties have been explored in lead-free materials. For example, giant piezoelectric constant d_{33} of 755 pC/N and d^*_{33} of 2027 pm/V were achieved in highly textured $BaTiO_3$-based ceramics [4]. Ultrahigh discharge energy density of 10.5 J/cm^3 and efficiency of 87% were obtained in $BiFeO_3$–$BaTiO_3$ ceramic multilayers [5]. In particular, exploring lead-free ferroelectric materials with large strain is of great significance for developing transducers. As one of lead-free materials, $(Bi_{0.5}Na_{0.5})TiO_3$ (BNT)-based ceramics are particularly attractive because Bi^{3+} and Pb^{2+} have similar electron configurations with $6s^2$ [6]. Among BNT-based ceramics, $Bi_{0.5}Na_{0.5}TiO_3$–$Bi_{0.5}K_{0.5}TiO_3$ (BNKT) solid solutions have been concerned intensively due to the relaxor ferroelectric behavior with high electromechanical properties. The BNKT-based ceramics are often accompanied by relatively

Address correspondence to E-mail: xmchen@snnu.edu.cn; guangbinzhang@snnu.edu.cn

https://doi.org/10.1007/s10854-020-04305-7

high strain under an appropriate electric field. For instance, a large field-induced strain up to 0.438% at a low electric field of 5 kV/mm was obtained in Nb^{5+}-doped BNKT-based ceramics due to the reversible phase transition between an ergodic relaxor (ER) phase to a ferroelectric (FE) phase [7]. Tan et al. studied the same system and achieved a giant strain of 0.7% via the two-step sintering method [8]. Zhou et al. reported a high strain of 0.32% with good temperature insensitivity in the same system [9]. The long-range ferroelectric domains could be decomposed into active polar nanoregion (PNRs) by appropriate chemical modification, which could be transformed into an unstable polar ferroelectric order under external electric fields, and reverted back to the virgin state after removal of the electric fields [9, 10]. Meanwhile, the highly asymmetric strain behavior caused by strong internal bias field should be avoided [11].

The ceramics $BiMO_3$ (M = Al^{3+}, Fe^{3+}, Ga^{3+}, In^{3+}, etc.) have large remanent polarization and high Curie temperature [12, 13]. $BiAlO_3$ has been paid much attention due to its good ferroelectric properties as well as relatively inexpensive constituent elements [14]. Furthermore, the electric charge of Al^{3+} is stable. It has been reported that $BiAlO_3$ shows rhombohedral perovskite symmetry, high Curie temperature (527 °C), and large spontaneous polarization ($\sim$ 76 $\mu C/cm^2$) [15, 16]. $BiAlO_3$ has been added into BNT-based ceramics to tune microstructure and electrical properties. Fu et al. synthesized $(1-x)Bi_{0.5}(Na_{0.82}K_{0.18})_{0.5}TiO_3$–$xBiAlO_3$ ceramics with decreased grain sizes and improved ferroelectric properties [17]. Shi et al. fabricated $(1-x)(0.72Bi_{0.5}Na_{0.5}TiO_3$–$0.28SrTiO_3)$–$xBiAlO_3$ ceramics and showed that dielectric constant and piezoelectric coefficient decreased with the increase in $BiAlO_3$ content because of relaxor behavior [18]. Wang et al. reported the influence of the doping amount of $BiAlO_3$ on microstructure and electrical properties of $(1-x)(0.93Bi_{0.5}Na_{0.5}TiO_3$–$0.07BaTiO_3)$–$xBiAlO_3$ ceramics and found that the addition of $BiAlO_3$ could effectively disrupt ferroelectric order and led to a degradation of the remanent polarization and coercive field [19]. It is also reported that the addition of $BiAlO_3$ into BNKT significantly disrupted ferroelectric order and enhanced strain due to the formation of a ferroelectric-relaxor phase boundary [14–16, 20].

As demonstrated above, $BiAlO_3$ is one of important chemical modifiers. In order to tune dielectric and ferroelectric behavior, $(1-x)(Bi_{0.5}Na_{0.42}K_{0.08})_{0.96}Sr_{0.04}Ti_{0.975}Nb_{0.025}O_3$–$xBiAlO_3$ (BNKTBA/x) lead-free ceramics were prepared by means of the solid-state reaction method. The effects of $BiAlO_3$ on phase structure, microstructure, dielectric properties, and ferroelectric properties of the ceramics were systematically studied.

2 Experimental procedure

The $(1-x)(Bi_{0.5}Na_{0.42}K_{0.08})_{0.96}Sr_{0.04}Ti_{0.975}Nb_{0.025}O_3$–$xBiAlO_3$ (BNKTBA/x, x = 0, 0.01, 0.02, 0.03, 0.05) ceramics were achieved via the traditional solid-state reaction method using powders Na_2CO_3 (99.8%), Bi_2O_3 (98.9%), K_2CO_3 (99%), Nb_2O_5 (99.5%), $SrCO_3$ (99%), TiO_2 (98.0%), and Al_2O_3 (99.99%) as starting raw materials. The powders were baked at 120 °C for 24 h before weighing. Each raw material was weighed according to the chemical formula and their mixture were ball-milled for 24 h in ethanol with zirconia balls, and then calcined at 850 °C for 3 h after drying. The calcined powders were ball-milled for 12 h again. After drying, the powders were compacted into pellets with the size of 1.2 mm in thickness and 10 mm in diameter under cold isostatic press 200 Mpa for 5 min. The pellets were buried in the powders with the same composition in an alumina crucible and then sintered at 1145 °C for 3 h.

Bulk densities of the sintered pellets were determined according to the Archimedes method. Phase structure of the ceramics was measured using an X-ray diffraction instrument (XRD, Rigaku D/Max 2550). Lattice parameters were extracted based on the XRD data by means of the software Jade 6. Microstructure of the ceramics was investigated with the Nova Nano 450 scanning electron microscope (SEM, FEI). For measuring SEM images, the fractured surfaces of the ceramics were polished and then thermally etched at 945 °C for 30 min.

Silver electrodes were coated on both polished sample surfaces and heated at 650 °C for 30 min. Ferroelectric behavior including polarization hysteresis loops and strain curves were recorded using a ferroelectric measurement system (Radiant Technologies Inc., Albuquerque, NM). The samples were poled at 50 kV/cm for 30 min at room temperature. Piezoelectric constant d_{33} of each poled ceramic was measured using a quasi-static d_{33} meter (ZJ-4A).

Dielectric spectra were measured by means of an Agilent E4980A LCR meter.

3 Results and discussion

The XRD curves for the BNKTBA/x ceramics are displayed in Fig. 1a. All of the ceramics have ABO_3 perovskite structure. Some secondary peaks are visible on the XRD curves of the samples with $x > 0$. These additional XRD peaks can be attributed to the reaction products between Al^{3+} and Bi^{3+}, such as $Bi_2Al_4O_9$ [14, 15, 21, 22] and $Bi_{48}Al_2O_{75}$ [16], which are always observed in the $BiAlO_3$-doped BNT-based ceramics [14–16, 21–23]. The position of the XRD peaks shifts towards high angle direction as x increases from 0 to 0.02 (Fig. 1b), indicating contraction of the lattice. All the ceramics exhibit pseudocubic symmetry, which can be indexed according to the JCPDS No. 89-3109 [24]. Based on the JCPDS No. 89-3109, the extracted lattice parameters a are 3.909(6) Å, 3.907(7) Å, 3.903(8) Å, 3.905(2) Å, and 3.905(1) Å for the samples with x = 0, 0.01, 0.02, 0.03, and 0.05, respectively. The radius of Al^{3+} (0.535 Å, coordination number CN = 6) is smaller than that of Ti^{4+} (0.605 Å, CN = 6) or Nb^{5+} (0.64 Å, CN = 6). The entrance of Al^{3+} into the B-site will cause contraction of the lattice due to the smaller radius of Al^{3+}. For the ceramics with $x \geq 0.03$, the XRD peaks almost do not shift with increasing x, implying that no more Al^{3+} ions entered into these samples.

The bulk densities of the BNKTBA/x (x = 0, 0.01, 0.02, 0.03, and 0.05) ceramics are 5.72, 5.75, 5.80, 5.83, and 5.81 g/cm^3, respectively, corresponding to the relative densities higher than 96.5% (the theoretical density of 5.92 g/cm^3 roughly used for all the samples). Figure 2 shows SEM images of fractured surfaces of the polish and thermally etched ceramics. The dense microstructures have been developed and almost no pores can be found in the bulk of the ceramics, coinciding with the high relative densities.

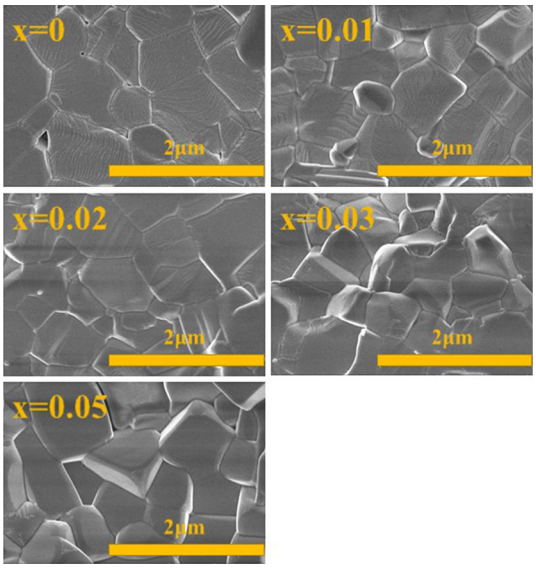

Fig. 2 SEM images of fractured surfaces of the polish and thermally etched ceramics

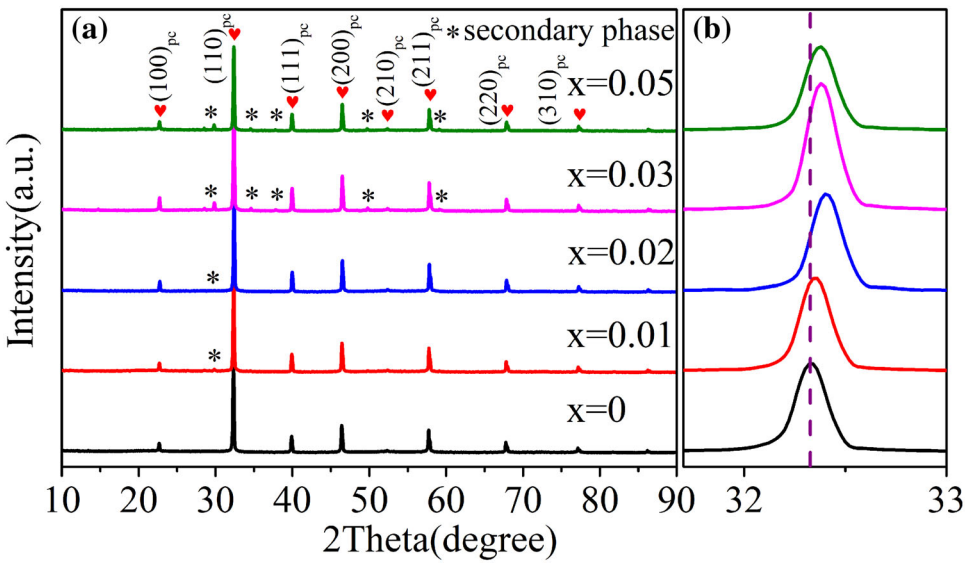

Fig. 1 XRD curves of the ceramics (**a**); magnified pattern around 30° (**b**). The peaks were indexed via JCPDS No. 89-3109 with pseudocubic (pc) indices

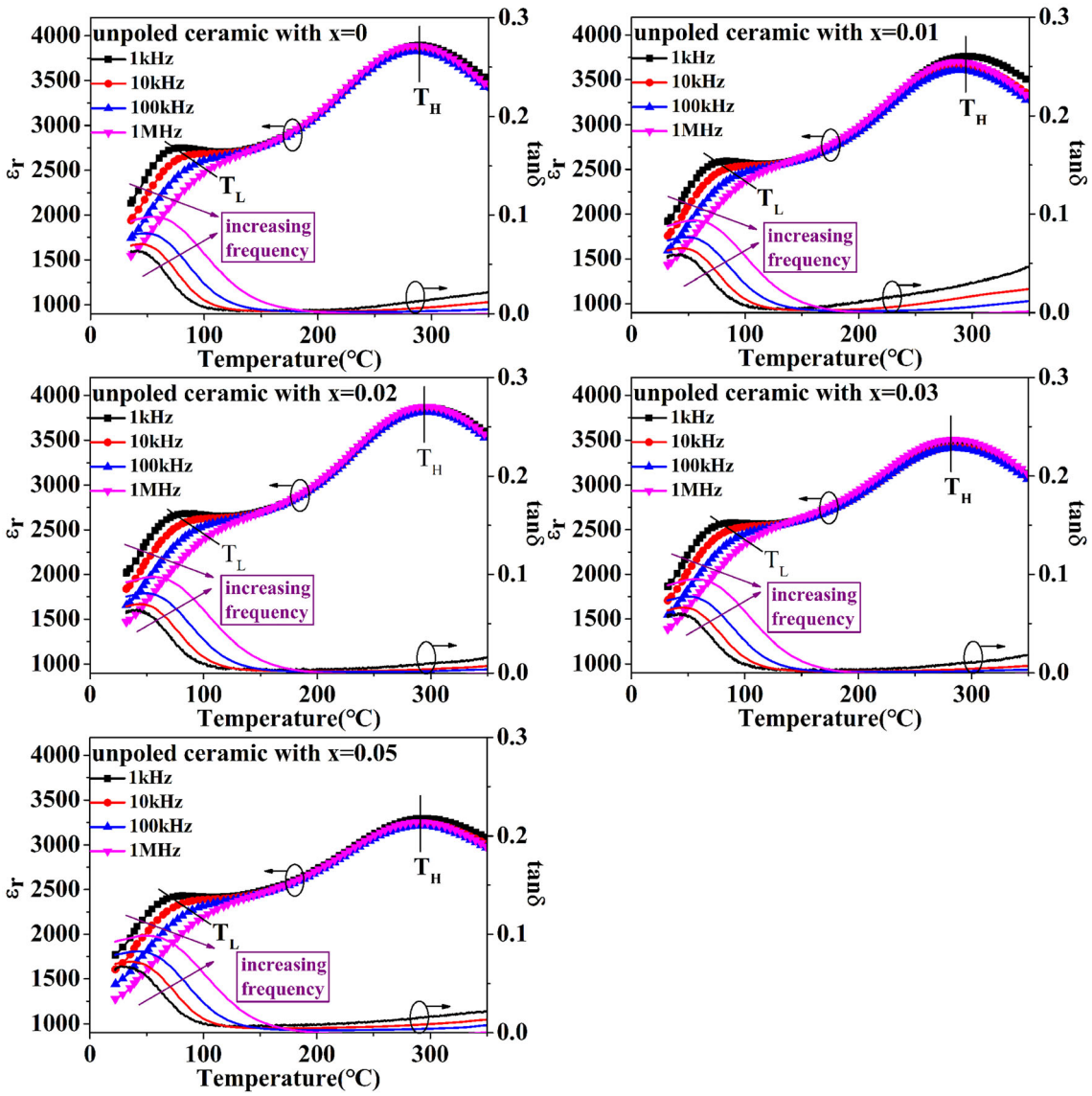

Fig. 3 Dielectric constant (ε_r) and dielectric loss (tanδ) vs. temperature at frequencies of 1 kHz, 10 kHz, 100 kHz, and 1 MHz for the unpoled ceramics

The dielectric constant (ε_r) values of the ceramics at 25 °C and 1 kHz are 1889, 1799, 1882, 1740, and 1776 for x = 0, 0.01, 0.02, 0.03, and 0.05, respectively. The corresponding dielectric loss (tanδ) values are 0.06, 0.05, 0.06, 0.05, and 0.06, respectively. The temperature-dependent ε_r and tanδ of the unpoled ceramics are displayed in Fig. 3. All of the dielectric constant ~ temperature curves present two dielectric anomalies. The shoulder locating at the low-temperature side is denoted as T_L. The peak at the high-temperature side is denoted as T_H. For all of the samples, there appears frequency dispersion of dielectric constant around T_L. As temperature further increases to T_H, the values of dielectric constant at different frequencies tend to be same. At temperature higher than T_H, frequency dispersion of dielectric constant appears again. The similar phenomena are always reported in BNT-based system [25–28]. The two dielectric anomalies are related to thermal evolution of polar nanoregions (PNRs) with different structural symmetry [26–28]. The temperature T_H is always used to determine Curie temperature in BNT-based ceramics [3]. The values of T_H change slightly for the ceramics with x = 0, 0.01, 0.02, 0.03, and 0.05, which are 290 °C, 296 °C, 299 °C, 284 °C, and 296 °C, respectively. The dielectric constant at T_H is denoted

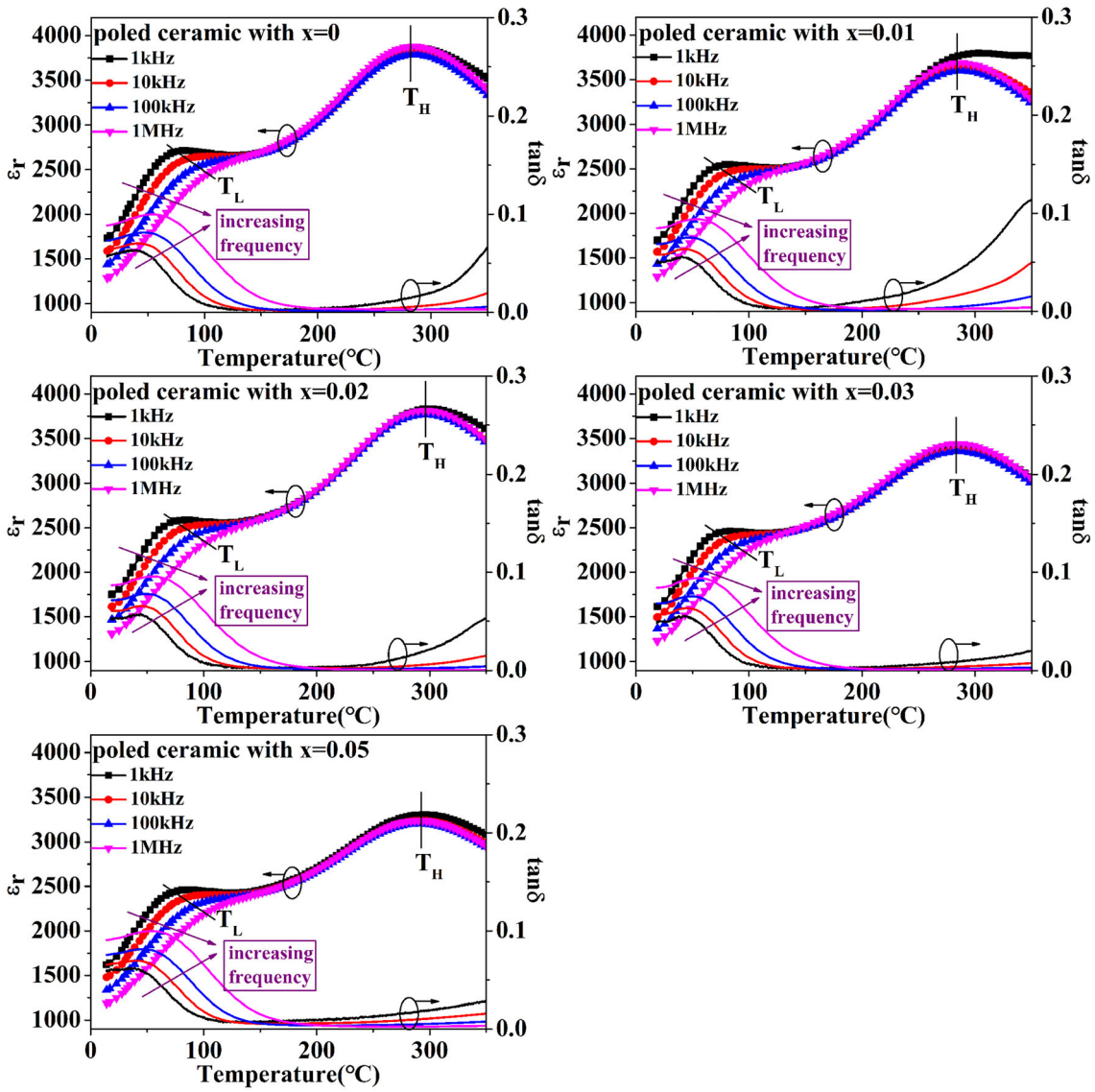

Fig. 4 Dielectric constant (ε_r) and dielectric loss (tanδ) vs. temperature at frequencies of 1 kHz, 10 kHz, 100 kHz, and 1 MHz for the poled ceramics

as ε_m. The ε_m values of the ceramics are 3892, 3766, 3863, 3449, and 3296 for x = 0, 0.01, 0.02, 0.03, and 0.05, respectively. In the temperature range between approximate 150 °C and T_H, the changes in dielectric constant with increasing measurement temperatures become gentle for the ceramics with the high doping amounts due to the decrease of ε_m. For a given difference in ε_r between 150 °C and a given temperature T_x (denoted as $\Delta\varepsilon_r = \varepsilon_{r,150} - \varepsilon_{r,T_x}$), the temperature window from 150 °C to T_x becomes wider with an increase in $BiAlO_3$ amount, in which $\varepsilon_{r,150}$ is dielectric constant at 150 °C, $\varepsilon_{r,Tx}$ is the dielectric constant at T_x. For example, when $\Delta\varepsilon_r$ = 500, the T_x values are 214 °C, 216 °C, 219 °C, 223 °C, and 232 °C for x = 0, 0.01, 0.02, 0.03, and 0.05, respectively. The corresponding values of temperature window are 64 °C, 66 °C, 69 °C, 73 °C, and 82 °C, respectively. Moreover, in this temperature range, dielectric loss is stable with changing temperature. The doping of $BiAlO_3$ is beneficial to temperature stability of ε_r and tanδ in the high-temperature region.

All of the ceramics were poled at room temperature under 50 kV/cm. The electric field of 50 kV/cm is much larger than the values of coercive field (as shown in Fig. 7). The electric field is enough for poling BNT-based ceramics, as also reported

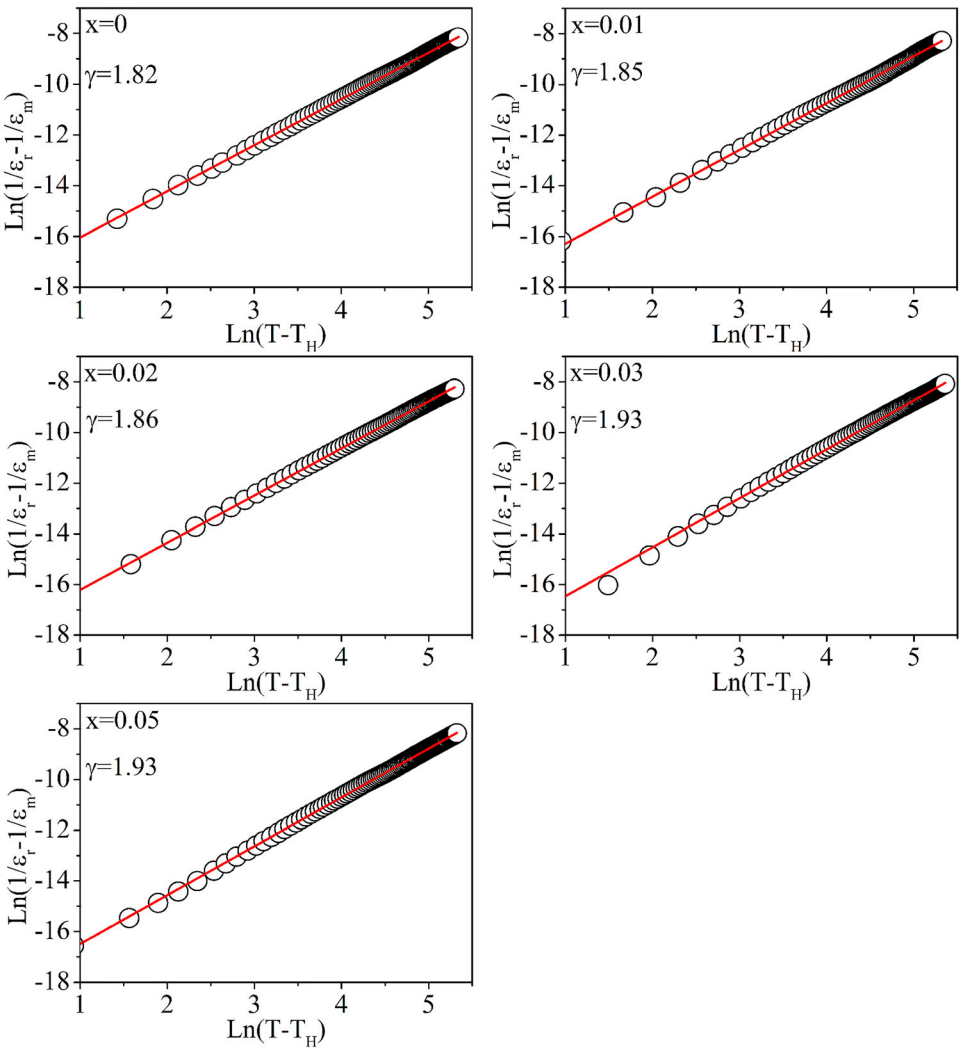

Fig. 5 Plots of $\mathrm{Ln}(1/\varepsilon_r - 1/\varepsilon_m)$ vs. $\mathrm{Ln}(T - T_H)$. The symbols denote experimental data measured at 10 kHz, while the solid lines denote the least-square fitting curves via the modified Curie–Weiss law

elsewhere [29, 30]. However, all of the poled ceramics exhibit piezoelectric constant d_{33} values close to 0. According to the thermodynamic theory of ferroelectrics [31], d_{33} is proportional to remnant polarization P_r:

$$d_{33} = 2Q_{11} \times P_r \times \varepsilon_{33}^{T}, \quad (1)$$

where Q_{11} represents the electrostrictive coefficient that is constant for a given perovskite material; ε_{33}^{T} represents dielectric constant of the material. As shown in Fig. 7, the P_r values under 50 kV/cm are 3.22 μC/cm^2, 4.13 μC/cm^2, 3.41 μC/cm^2, 3.63 μC/cm^2, and 7.24 μC/cm^2 for x = 0, 0.01, 0.02, 0.03, and 0.05, respectively. The ceramics exhibit low P_r values, which should correspond to the very low d_{33} values.

Figure 4 shows the temperature (T)-dependent ε_r and tanδ of the poled ceramics. As can be seen, the changes of ε_r with increasing temperature for the poled samples are almost as same as those for the unpoled samples (Fig. 3). It has been widely reported that there always appears a T_d anomaly on the dielectric spectra for the poled BNT-based ceramics, where T_d is defined as the temperature corresponding to a sharp peak on the tanδ–T curves and the steepest increase on the ε_r–T curves [25, 29, 32]. T_d is the temperature where an electric field-induced long-range ferroelectric order reverts back to the initial relaxor state upon heating, which marks the depolarization [27, 33]. However, for the present poled samples, no T_d anomaly was observed on the dielectric spectra. The results suggest that depolarization occurs for the poled samples at room temperature. The results are consistent with the ferroelectric characteristic of the samples, as shown later.

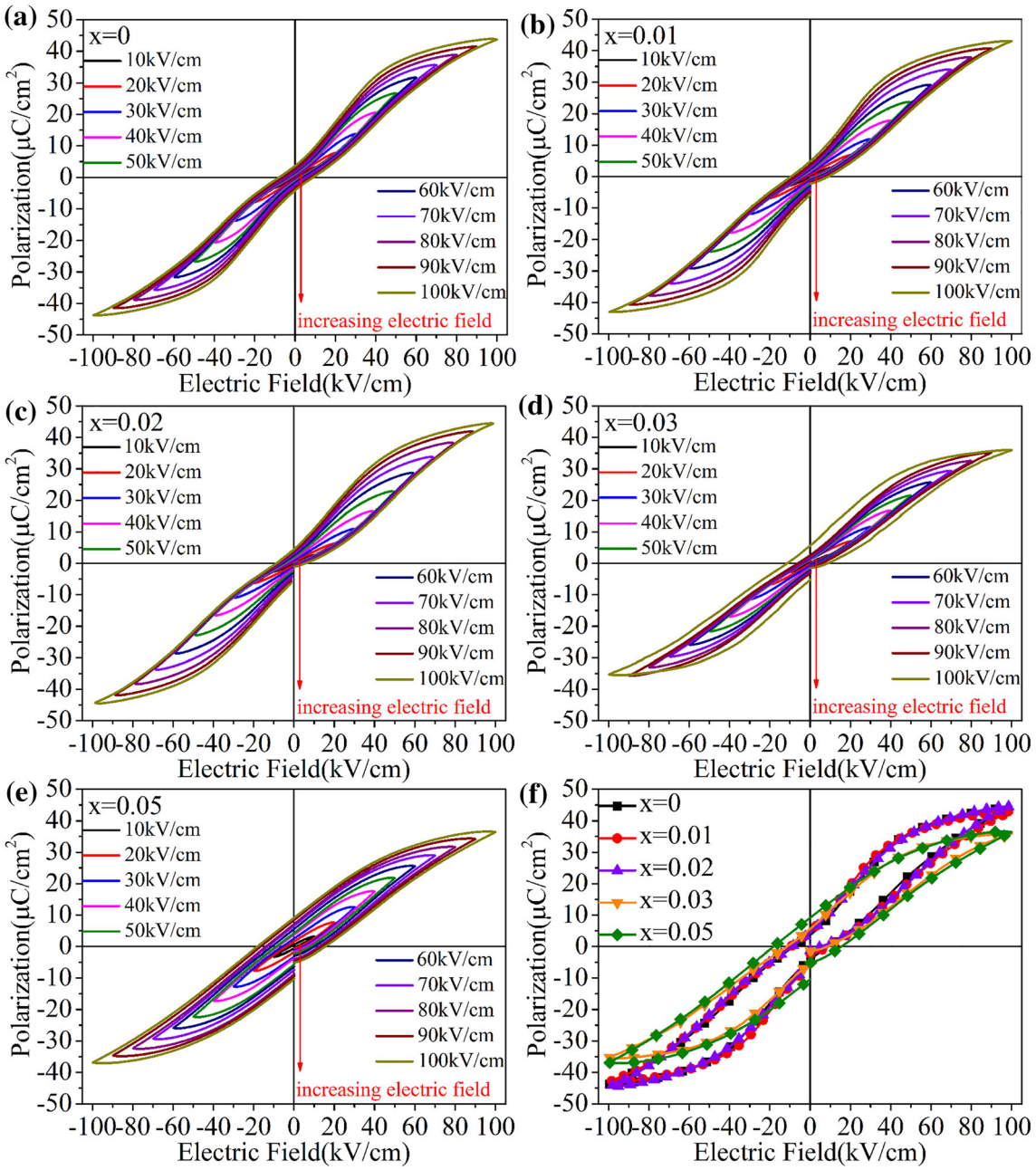

Fig. 6 *P–E* loops of the ceramics under various electric fields (**a**–**e**); *P–E* loops of the ceramics measured at 100 kV/cm (**f**)

The diffuse character around T_H was studied according to the modified Curie–Weiss law [34]:

$$\frac{1}{\varepsilon_r} - \frac{1}{\varepsilon_m} = \frac{(T - T_H)^\gamma}{C}, \quad (2)$$

where C is Curie-like constant, ε_m is the maximum dielectric constant at T_H, and γ is the degree of diffuseness. In general, the value of γ ranges from 1 to 2, corresponding to a typical ferroelectric to an ideal relaxor ferroelectric. Figure 5 demonstrates the fitting lines of $\mathrm{Ln}(1/\varepsilon_r - 1/\varepsilon_m)$ as a function of $\mathrm{Ln}(T - T_H)$. The γ values of the ceramics are 1.82, 1.85, 1.86, 1.93, and 1.93 for x = 0, 0.01, 0.02, 0.03, and 0.05, respectively. Obviously, the values of γ are close to 2, suggesting diffusion characteristic around T_H for all of the samples. The diffuse character of dielectric behavior in BNT-based ceramics is associated with the existence of complex cations, which possess similar radii but different charges and electronic configurations at an equivalent crystallographic site

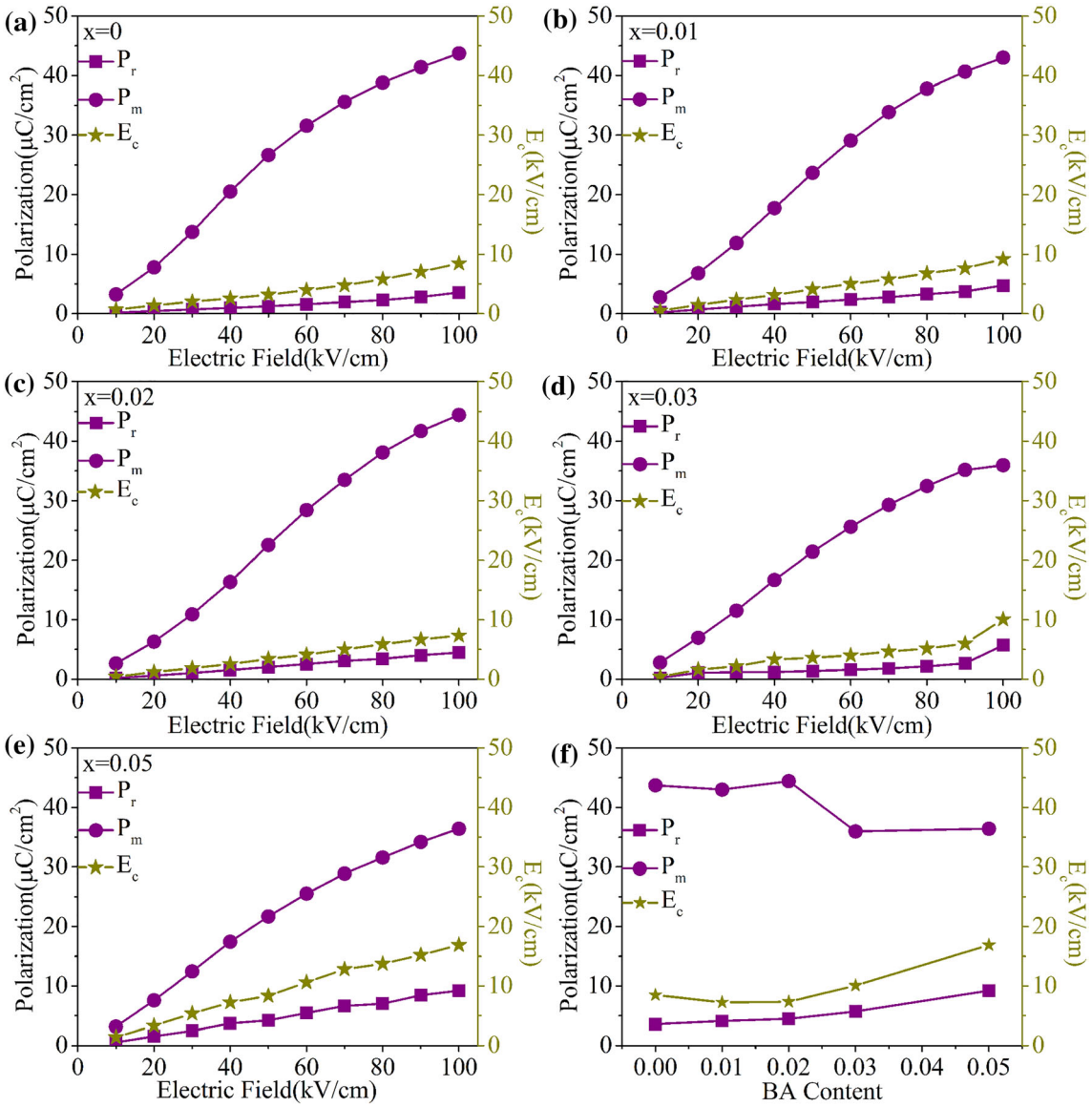

Fig. 7 The values of P_m, P_r, and E_c of the ceramics under the measurement electric fields from 10 kV/cm to 100 kV/cm (**a**–**e**); the values of P_m, P_r, and E_c of the ceramics at 100 kV/cm (**f**)

[35–37]. With the increase in $BiAlO_3$ doping content, more dopants enter into the crystallite site, causing an increase in the γ values.

The polarization (P)–electric field (E) loops of the ceramics under different electric fields (10 kV/cm–100 kV/cm) measured at room temperature are presented in Fig. 6a–e. The P–E loops display pinching-type shape under various measurement electric fields. The similar observation has been reported in other BNT-based ceramics [28, 38, 39]. Lim et al. attributed this behavior to the existence of pseudocubic phase [40]. Fan et al. argued that the pinched loops are always accompanied by the absence of T_d on the ε_r–T curves, which is related to ergodic relaxor nature [41]. For the present poled ceramics, there is no T_d anomaly on the dielectric spectra (Fig. 4). The dielectric behavior implies that no long-range ferroelectric order exists in the samples at room temperature. The doping of various ions into the BNT lattice, including K^+, Sr^{2+}, Nb^{5+}, and Al^{3+}, can disrupt the long-range ferroelectric order and result in ergodic relaxor phase, causing the pinched P–E loops [42–44]. The remnant polarization (P_r), maximum polarization (P_m), and coercive field (E_c) values as a function of measurement electric fields for all the samples are shown in Fig. 7a–e. For a given sample, the P_m, P_r,

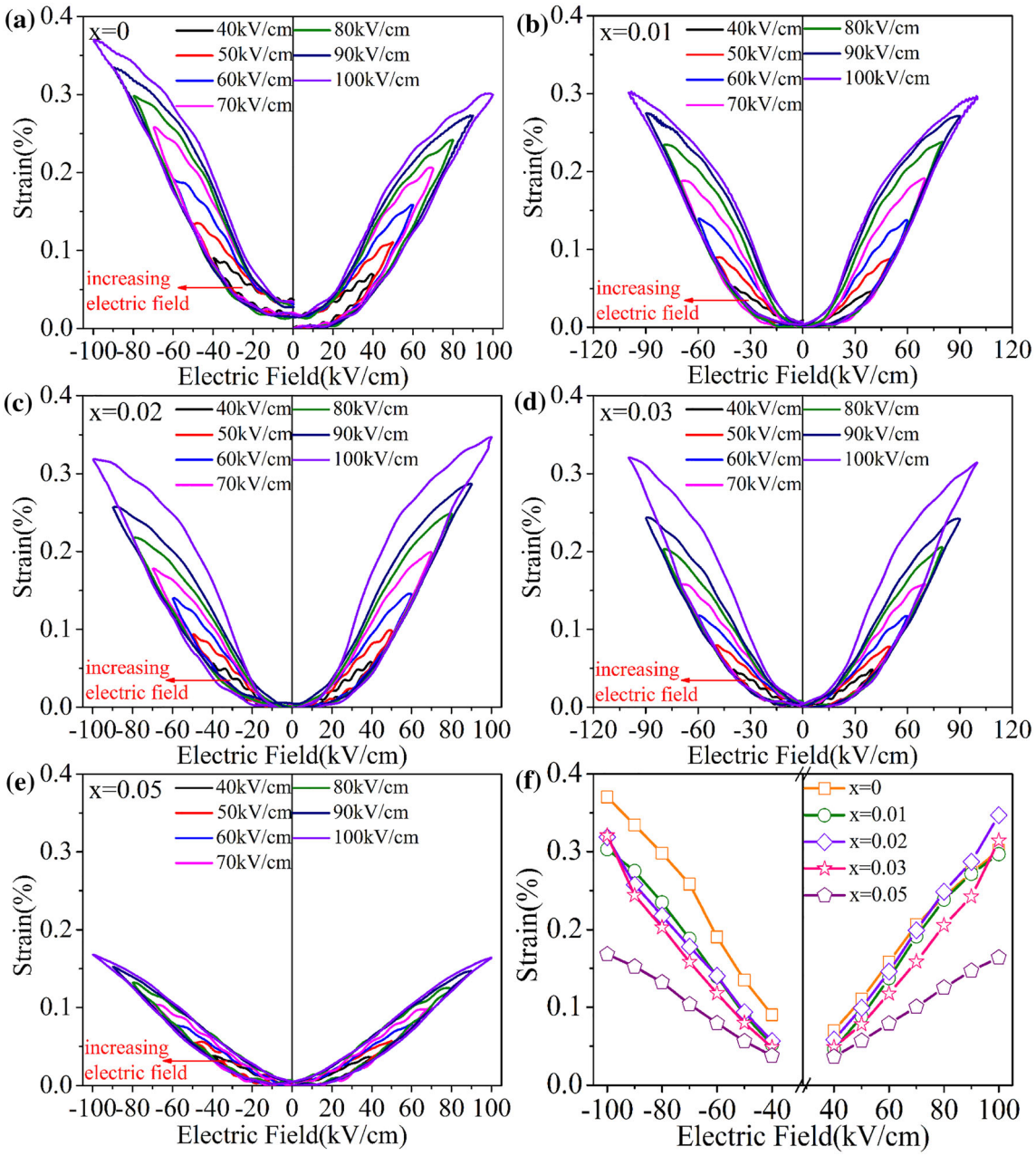

Fig. 8 Bipolar *S*–*E* loops of the ceramics at room temperature under various measurement electric fields from 40 to 100 kV/cm (**a**–**e**); maximum strain values under positive electric fields (S_m^+) and negative electric fields (S_m^-) as a function of measurement electric fields (**f**)

and E_c values increase with an increase in measurement electric fields. The increase of P_m from 10 to 100 kV/cm is more remarkable compared to the changes of P_r and E_c, demonstrating electric field-induced increment of polarization. The ceramics with x = 0, 0.01, and 0.02 exhibit gentle variation in P_r and E_c during the whole range of the measurement electric fields. The increases of P_r and E_c become obvious at the high electric fields for the ceramic with x = 0.03 (≥ 90 kV/cm). The ceramic with x = 0.05 shows significant increase in P_r and E_c during the whole measurement electric fields compared to the other samples. The *P*–*E* loops of the ceramics measured at 100 kV/cm are compared in Fig. 6f, and the corresponding P_m, P_r, and E_c values are shown in Fig. 7f. The P_m values show a downward trend with the increase of x and reach a maximum value (44.43 μC/cm^2) at x = 0.02. The change of P_r for the ceramics

from $x = 0$ to 0.02 is not significant, and the value increases from 3.59 to 4.48 μC/cm^2; the increase of P_r is more obvious for the ceramics from $x = 0.02$ to 0.05, which changes from 4.48 to 9.21 μC/cm^2. Accordingly, the E_c values show decreasing trend from 8.48 to 7.35 kV/cm as x changes from 0 to 0.02. As x changes from 0.02 to 0.05, the E_c values increase from 7.35 to 16.89 kV/cm. Among the samples, the ceramic shows relatively low P_r of 4.48 μC/cm^2, highest P_m of 44.43 μC/cm^2, and lowest E_c of 7.35 kV/cm at $x = 0.02$.

Figure 8a–e shows the bipolar electric field-induced strain (*S*–*E*) curves of the ceramics under various electric fields (40 kV/cm–100 kV/cm) measured at room temperature. For all the samples, the *S*–*E* hysteresis loops are sprout-shaped and negative strain is almost absent. The strain curves of the samples with $x \leq 0.03$ are similar, while the ceramic exhibits slender strain curves at $x = 0.05$. Figure 8f exhibits the maximum strain values under positive electric fields (S_m^+) and negative electric fields (S_m^-) as a function of measurement electric fields. It is evident that the electric-induced strain strongly depends on the applied electric fields and the strain values increase continuously with an increase in the electric fields for a given sample. The *S*–*E* loops of the sample with $x = 0$ are slightly asymmetric, causing a difference in S_m^+ and S_m^- at a given measurement electric field. The asymmetry is always attributed to the presence of internal bias field (E_i) [8, 45]. The values of E_i can be calculated via the formula $E_i = |E_{c+}| - |E_{c-}|$, in which E_{c+} and E_{c-} are electric fields at which the polarization values equal to zero under positive electric field and negative electric field, respectively. For example, the E_{c+} and E_{c-} values are 9.15 kV/cm and − 7.81 kV/cm for $x = 0$ at 100 kV/cm, respectively; so, the value of E_i is 1.34 kV/cm. In addition, compared to the rapid growth of strain values with increasing E for the samples with low doping content, the growth trend of strain values is obviously slow for the sample with $x = 0.05$, which is contrary to the variation trends of P_r and E_c with changing E (Fig. 8f). The ceramic shows the S_m^+ and S_m^- values of 0.35% and 0.32% under 100 kV/cm for $x = 0.02$, respectively. The ceramic with $x = 0.05$ shows the smallest strain values, which are 0.16% and 0.17% for S_m^+ and S_m^-, respectively. The relatively high strain performance for the samples with low doping amount should be related to the coexistence of FE and ER phases [41, 46, 47].

4 Conclusions

Lead-free ceramics BNKTBA/x with dense microstructures were successfully fabricated by means of the conventional solid-state reaction method. The influence of the $BiAlO_3$ doping on dielectric and ferroelectric properties was investigated. All of the ceramics present pseudocubic structure. For a given sample, whether it is poled or not, two dielectric anomalies are observed on the dielectric spectra and no T_d anomaly is observed in the studied temperature range. The doping of BA induces relaxor character, resulting in pinched-shape *P*–*E* and sprout-shape *S*–*E* hysteresis loops. The ceramic BNKTBA/0.02 shows the relatively low P_r of 4.48 μC/cm^2, the highest P_m of 44.43 μC/cm^2, lowest E_c of 7.35 kV/cm, and large S_m^+ of 0.35%.

Acknowledgements

This work was supported in part by National Natural Science Foundation of China (No. 51972202) and Fundamental Research Funds for the Central Universities (No. GK201901005).

References

1. J. Rődel, K.G. Webber, R. Dittmer, W. Jo, M. Kimura, D. Damjanovic, J. Eur. Ceram. Soc. **35**, 1659 (2015)
2. J.L. Xu, H. Deng, Z. Zeng, Z. Zhang, K.Y. Zhao, J.W. Chen, N. Nakamori, F.F. Wang, J.P. Ma, X.B. Li, H.S. Luo, Appl. Phys. Lett. **112**, 182901 (2018)
3. Y.C. Wu, G.S. Wang, Z. Jiao, Y.Z. Fan, P. Peng, X.L. Dong, RSC Adv. **9**, 21355 (2019)
4. Y.C. Liu, Y.F. Chang, F. Li, B. Yang, Y. Sun, J. Wu, S.T. Zhang, R.X. Wang, W.W. Cao, ACS Appl. Mater. Inter. **9**, 29863 (2017)
5. G. Wang, J.L. Li, X. Zhang, Z.M. Fan, F. Yang, A. Feteira, D. Zhou, D.C. Sinclair, T. Ma, X.L. Tan, D.W. Wang, I.M. Reaney, Energy Environ. Sci. **12**, 582 (2019)
6. R.A. Malik, A. Hussain, M. Acosta, J. Daniels, H.S. Han, M.H. Kim, J.S. Lee, J. Eur. Ceram. Soc. **38**, 2511 (2018)
7. R.A. Malik, J.K. Kang, A. Hussain, C.W. Ahn, H.S. Han, J.S. Lee, Appl. Phys. Express **7**, 061502 (2014)
8. X.M. Liu, X.L. Tan, Adv. Mater. **28**, 574 (2016)

9. X.F. Zhou, Z.N. Yan, H. Qi, L. Wang, S.Y. Wang, Y. Wang, C. Jiang, H. Luo, D. Zhang, J. Eur. Ceram. Soc. **39**, 2310 (2019)
10. D.S. Yin, Z.H. Zhao, Y.J. Dai, Z. Zhao, X.W. Zhang, S.H. Wang, J. Am. Ceram. Soc. **99**, 2354 (2016)
11. T.Y. Li, X.J. Lou, X.Q. Ke, S.D. Cheng, S.B. Mi, X.J. Wang, J. Shi, X. Liu, G.Z. Dong, H.Q. Fan, Y.Z. Wang, X.L. Tan, Acta Mater. **128**, 337 (2017)
12. T. Wang, X.M. Chen, Y.Z. Qiu, Ferroelectrics **510**, 161 (2017)
13. R. McQuade, T. Rowe, A. Manjon-Sanz, L. de la Puente, M.R. Dolgos, J. Alloys Compd. **762**, 378 (2018)
14. A. Ullah, C.W. Ahn, A. Hussain, S.Y. Lee, I.W. Kim, J. Am. Ceram. Soc. **94**, 3915 (2011)
15. A. Ullah, C.W. Ahn, A. Hussain, S.Y. Lee, I.W. Kim, Curr. Appl. Phys. **10**, 1174 (2010)
16. A. Ullah, C.W. Ahn, A. Hussain, I.W. Kim, H.I. Hwang, N.K. Cho, Solid State Commun. **150**, 1145 (2010)
17. P. Fu, Z.J. Xu, R.Q. Chu, X.Y. Wu, W. Li, M.J. Zhao, J. Alloys Compd. **535**, 5 (2012)
18. P. Shi, L.G. Zhu, W.W. Gao, Z.H. Yu, X.J. Lou, X.J. Wang, Z.M. Yang, S. Yang, J. Alloys Compd. **784**, 788 (2019)
19. J. Wang, X.M. Chen, X.M. Zhao, X.X. Liang, J.P. Zhou, P. Liu, Mater. Res. Bull. **67**, 94 (2015)
20. T. Zheng, J.G. Wu, D.Q. Xiao, J.G. Zhu, Prog. Mater. Sci. **98**, 552 (2018)
21. H.C. Yu, Z.G. Ye, Appl. Phys. Lett. **93**, 112902 (2008)
22. Z. Liu, W.J. Ren, P. Peng, S.B. Guo, T. Lu, Y. Liu, X.L. Dong, G.S. Wang, Appl. Phys. Lett. **112**, 142903 (2018)
23. Z.L. Yu, Y.F. Liu, M.Y. Shen, H. Qian, F.F. Li, Y.N. Lyu, Ceram. Int. **43**, 7653 (2017)
24. Joint Committee on Powder Diffraction Standards-International Center for Diffraction Data (JCPDS-ICDD) Card (2002)
25. H.S. Han, W. Jo, J. Rődel, I.K. Hong, W.P. Tai, J.S. Lee, J. Phys. Condens. Mater. **24**, 365901 (2012)
26. X.S. Qiao, X.M. Chen, H.L. Lian, J.P. Zhou, P. Liu, J. Eur. Ceram. Soc. **36**, 3995 (2016)
27. W. Jo, S. Schaab, E. Sapper, L.A. Schmitt, H.J. Kleebe, A.J. Bell, J. Rődel, J. Appl. Phys. **110**, 074106 (2011)
28. C. Wang, T.D. Xia, X.J. Lou, Ceram. Int. **44**, 7378 (2018)
29. R.Y. Jing, X.M. Chen, H.L. Lian, X.S. Qiao, X.J. Shao, J.P. Zhou, J. Eur. Ceram. Soc. **38**, 3111 (2018)
30. J.P. Ma, X.M. Chen, H.L. Lian, Q. Zhang, J.Q. Liu, J. Eur. Ceram. Soc. **39**, 264 (2019)
31. M.J. Haun, E. Furman, S.J. Jang, L.E. Cross, Ferroelectrics **99**, 13 (1989)
32. X.S. Qiao, X.M. Chen, H.L. Lian, W.T. Chen, J.P. Zhou, P. Liu, J. Am. Ceram. Soc. **99**, 198 (2016)
33. J. Zhang, Z. Pan, P.X. Nie, Y.S. Cui, B. Yang, J. Chen, S.T. Zhang, Appl. Phys. Lett. **106**, 232904 (2015)
34. W.P. Cao, J. Sheng, Y.L. Qiao, L. Jing, Z. Liu, J. Wang, W.L. Li, J. Eur. Ceram. Soc. **39**, 4046 (2019)
35. T. Wang, X.M. Chen, Y.Z. Qiu, H.L. Lian, W.T. Chen, Mater. Chem. Phys. **186**, 407 (2017)
36. L.N. Liu, X.M. Chen, R.Y. Jing, H.L. Lian, W.W. Wu, Y.P. Mou, P. Liu, J. Mater. Sci.: Mater. Electron. **30**, 5233 (2019)
37. R.Y. Jing, X.M. Chen, J.P. Ma, H.L. Lian, W.W. Chen, J. Mater. Sci. **53**, 574 (2018)
38. S. Manotham, P. Jaita, C. Randorn, G. Rujijanagul, D.P. Cann, J. Alloys Compd. **808**, 151655 (2019)
39. P. Jaita, R. Sanjoom, N. Lertcumfua, G. Rujijanagul, RSC Adv. **9**, 11922 (2019)
40. D.H. Lim, M. Saleem, I.S. Kim, M.S. Kim, B.K. Koo, S.J. Jeong, Sensors Actuators A **282**, 163 (2018)
41. P.Y. Fan, Y.Y. Zhang, B. Xie, Y.W. Zhu, W.G. Ma, C. Wang, B. Yang, J.L. Xu, J.Z. Xiao, H.B. Zhang, Ceram. Int. **44**, 3211 (2018)
42. R.A. Malik, A. Hussain, A. Maqbool, A. Zaman, C.W. Ahn, J.U. Rahman, T.K. Song, W.J. Kim, M.H. Kim, J. Am. Ceram. Soc. **98**, 3842 (2015)
43. X. Liu, J.W. Zhai, B. Shen, F. Li, Y. Zhang, P. Li, B.H. Liu, J. Eur. Ceram. Soc. **37**, 1437 (2017)
44. J.G. Hao, Z.J. Xu, R.Q. Chu, W. Li, J. Du, P. Fu, RSC Adv. **5**, 82605 (2015)
45. G. Du, R.H. Liang, L. Wang, K. Li, W.B. Zhang, G.H. Wang, X.L. Dong, Ceram. Int. **39**, 7703 (2013)
46. R.F. Cheng, Z.J. Xu, R.Q. Chu, J.G. Hao, J. Du, G.R. Li, J. Eur. Ceram. Soc. **36**, 489 (2016)
47. P.Y. Fan, Y.Y. Zhang, Q. Zhang, B. Xie, Y.W. Zhu, M.A. Mawat, W.G. Ma, K. Liu, J.Z. Xiao, H.B. Zhang, J. Eur. Ceram. Soc. **38**, 4404 (2018)